# CMS ECAL monitoring and calibration in LHC Run II

IOP Conf. Series: Journal of Physics: Conf. Series 1162 (2019) 012002 doi:10.1088/1742-6596/1162/1/012002

# CMS ECAL monitoring and calibration in LHC Run II

**Tanmay Mudholkar, on behalf of the CMS Collaboration**
CERN, Switzerland / Carnegie Mellon University, Pittsburgh, PA, U.S.A.
E-mail: tanmay.kamalakar.mudholkar@cern.ch

**Abstract.** The CMS electromagnetic calorimeter (ECAL) plays a crucial role in measurements of electrons and photons produced in LHC collisions at CMS. LHC continues to operate a highly successful data-taking program, having already delivered an integrated luminosity of more than 125 fb$^{-1}$ with $pp$ collisions since the beginning of Run II. With the expected degradation of ECAL crystals and electronics due to aging and radiation damage, it is essential to regularly fine-tune ECAL calibration factors at the highest possible granularity in order to maintain excellent energy resolution. In addition, it is important to maintain a continuous program of monitoring various physics quantities that depend on ECAL measurements, in order to validate the calibrations and ensure long-term reliability of the measurements. We describe the three techniques currently used to set the calibration factors at the crystal level: using the known energy scales in $\pi^0 \to \gamma\gamma$ and in $Z \to ee$ events, and comparing the energy measured by ECAL with an independent measurement of electron momentum from the Si tracker. We also describe the various physics quantities we monitor to validate the energy scale and shower shapes. Finally we provide an estimate of the improvement in the energy resolution after applying updated calibrations.

## 1. Introduction

The electromagnetic calorimeter (ECAL) of CMS [1] consists of a cylindrical section surrounding the central beam-pipe in the pseudorapidity range $|\eta| < 1.48$, and endcaps at both ends that extend the pseudorapidity coverage to $|\eta| < 3.0$.

The primary building-blocks of ECAL are scintillating lead tungstate crystals of which there are 61,200 in the barrel and 14,648 across both endcaps. Lead tungstate features a typical scintillation decay time of ∼25 ns, allowing very good time resolution. It has a short radiation length ($X_0 = 0.89$ cm); the ECAL crystals are about 23 cm, or about 25 $X_0$, in depth. The Molière radius of lead tungstate is small ($R_{\rm M} = 2.19$ cm). The transverse size of the crystals is $2.2 \times 2.2$ cm$^2$ in the barrel and $2.9 \times 2.9$ cm$^2$ in the endcaps; electromagnetic showers in ECAL are typically spread over multiple crystals.

These crystals are connected to photodetectors that detect the scintillation signal. In the barrel, the photodetectors are avalanche photodiodes (APDs), which operate at gain 50 in the full 3.8 T magnetic field. In the endcaps, the photodetectors are vacuum phototriodes (VPTs), which operate at gain 10 and are highly radiation tolerant.

In addition to the scintillating crystals, ECAL also contains 137,216 thin silicon strips with dimensions $2.0 \times 63 \times 0.3$ mm$^3$ in four planes in a sampling configuration (two planes in front of each endcap with coverage $1.65 < |\eta| < 2.6$), with lead plates of thickness 3 $X_0$ as the absorber.

Approximately 5% of the total energy deposited by an electromagnetic particle in the endcaps is absorbed by the preshower. The primary design purpose of the ECAL preshower is to achieve excellent spatial resolution in the endcaps, which is necessary to distinguish genuine high-energy photons from close photon pairs (for instance those resulting from $\pi^0$ decay). This is achieved by orienting the thin strips lengthwise along $x$ in one plane and along $y$ in the other plane in front of each ECAL endcap.

## 2. ECAL Monitoring and Calibration

The physics performance of LHC has been excellent throughout Run II. In 2018, LHC is regularly achieving stable operation at a luminosity of $2 \times 10^{34}\text{cm}^{-2}\text{s}^{-1}$, which is twice the design value, and the average number of concurrent proton-proton collisions per bunch crossing (pile-up) peaks at around 60. In order to ensure the continued reliability of the ECAL energy reconstruction in these challenging conditions, it is necessary to keep up-to-date all the factors that go into the overall energy reconstruction, and to monitor the reconstruction by examining its behavior in samples with well-understood physics events. The next subsection is a brief description of the reconstruction of electron and photon energies by ECAL.

### *2.1. ECAL energy reconstruction*

First an algorithm identifies a list of crystals (a "supercluster") in which an electromagnetic particle produced in the collision deposited energy. Electrons and positrons bend along the cylindrical $\phi$-coordinate with respect to the longitudinal magnetic field of CMS, and release bremsstrahlung photons spread in $\phi$, which are recovered by the supercluster algorithm [2] in addition to the photon conversion energy.

The reconstructed energy is then calculated as a sum over all crystals within this supercluster:

$$E_{e,\gamma} = F_{e,\gamma} \times \left[ G\left(\eta\right) \times \left\{ \sum_{i \in \text{SC}} S_i\left(t\right) \times C_i \times A_i \right\} + E_{\text{preshower}} \right] \tag{1}$$

Here, the factors $A_i$ are the raw pulse amplitudes in ADC as measured by the read-out electronics. A detailed description of the raw amplitudes can be found in [3]. $G\left(\eta\right)$ contains the ADC-to-GeV conversion factor allowing for an $\eta$-dependence to incorporate geometry effects. The factor $F_{e,\gamma}$ corrects for imperfect clustering and other geometry effects, and depends on the type of particle. For electrons and photons incident on the endcaps, $E_{\text{preshower}}$ contains an estimate of the energy absorbed in the lead planes, and section 4 discusses how the individual ECAL preshower sensors are calibrated. The inter-calibration coefficients $C_i$ allow us to set an energy scale at the granularity of a single crystal; the procedure for obtaining these coefficients is discussed in section 3. The factors $S_i\left(t\right)$ are discussed in the next subsection.

### *2.2. Crystal response to the scintillation signal*

The response of each ECAL crystal to a scintillation signal varies with time. There is a loss of transparency due to radiation damage; in general, as LHC provides higher luminosities each year, this loss is significant especially at high $\eta$. There is also a partial recovery of the transparency at room temperature. Fluctuations due to these trends affect the crystal response on short time-scales as well; the response of crystals to scintillation can vary significantly within an LHC fill. In order to monitor this response, ECAL operates a dedicated laser system [4] which shines laser light into all ECAL crystals and measures the response. For ECAL crystals, the scintillation signal drift $S$ is assumed to be related to the laser monitoring signal $L$ by a power law:

$$\frac{S}{S_0} = \left(\frac{L}{L_0}\right)^{\alpha} \tag{2}$$

The exponent $\alpha$ is measured to be 1.6; as described in [4], this single value of $\alpha$ allows the scintillation response to be monitored with good accuracy. While this procedure works well for short-term drifts in the response to the scintillation signal, there still remains a long-term residual drift that cannot be picked up by the laser monitoring. For example, $\alpha$ varies slightly from crystal to crystal, and there are residual aging effects that affect each crystal differently. To compensate for all these additional factors, we include the crystal-dependent inter-calibration coefficients $C_i$.

## 3. Inter-Calibration Coefficients

One method of calculating these inter-calibration coefficients is the $\phi-$symmetry method. In this method we exploit the azimuthal symmetry of minimum-bias events, which enables us to set the relative inter-calibration coefficients for crystals at the same $\eta$ (because these "minbias" events are highly sensitive to geometric effects, including some absorption in the tracker, the precision of the coefficients obtained using this technique is lower than that achieved with other available methods). Fig. 1 shows the drift in the barrel in 2016 of the inter-calibration coefficients, with respect to their value at the beginning of 2016 in blue, and with respect to their value at the previous measurement in red, as calculated using the $\phi$-symmetry technique. These plots show the necessity of deriving the inter-calibration coefficients at regular time intervals in order to maintain good energy resolution.

We currently use three independent techniques to calculate the inter-calibration coefficient for each crystal, and obtain a combined measurement as well as an estimate of the uncertainty due to each individual technique. These techniques are summarized briefly in the next few subsections. A detailed description of these techniques can be found in [5].

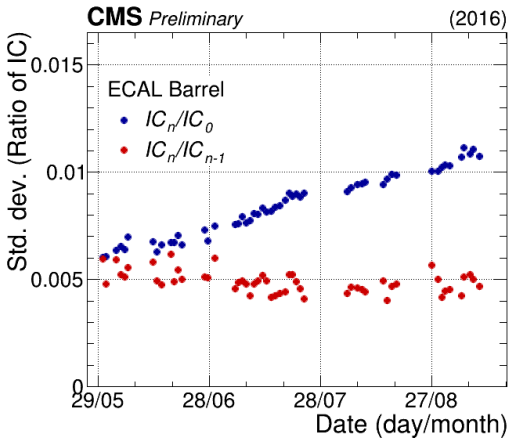


**Figure 1.** Drift of the inter-calibration coefficients in the barrel during 2016 data taking.

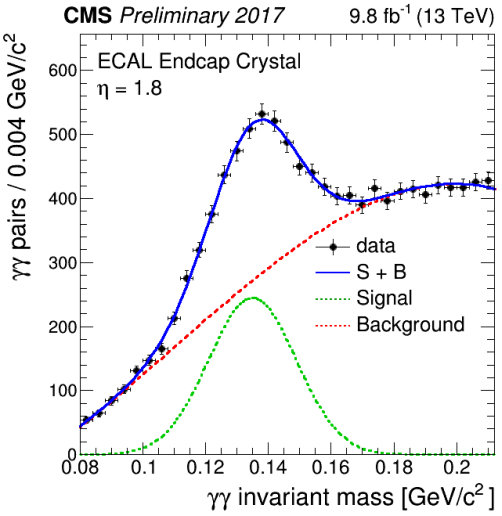


**Figure 2.** $m_{\gamma\gamma}$ distribution, fitted to the data, for a selected endcap crystal.

### *3.1. Inter-calibration using $\pi^0 \to \gamma\gamma$*

We use events in a special data stream from a dedicated trigger that selects diphoton events close to the $\pi^0$ invariant mass. For each crystal, we select events with one hit in that crystal, and fit the $\gamma\gamma$ invariant mass distribution separately with this selection. Because each fit depends on the inter-calibration coefficients of all crystals, the true values are obtained following an

iterative process in which the coefficients at iteration $n$ are obtained from the coefficients at iteration $n-1$; after a sufficicient number of iterations, the peak of the fitted distributions for all crystals converges to the PDG value of the $\pi^0$ mass. In [6] this technique is described for the $Z \to ee$ inter-calibrations, but it can be applied more generally to $\pi^0 \to \gamma\gamma$. At iteration $n$,

$$C_i = \prod_{\text{iteration}}^{n} \left[ 1 + \frac{1}{2} \left\{ \left( \frac{m^j_{\gamma\gamma}\,(\text{events with crystal i})}{m^{\text{PDG}}_{\gamma\gamma}} \right)^2 - 1 \right\} \right]^{-1} \quad (3)$$

Examples of the fitted distributions are shown in Fig. 2 for a selected endcap crystal. The final $C_i$ for a crystal is normalized to the $\eta-$ring average, because the $\eta-$scale correction is found to be much more precise when done with the $Z \to ee$ method described in section 3.3.

### *3.2. Inter-calibration using $E/p$ ratio*

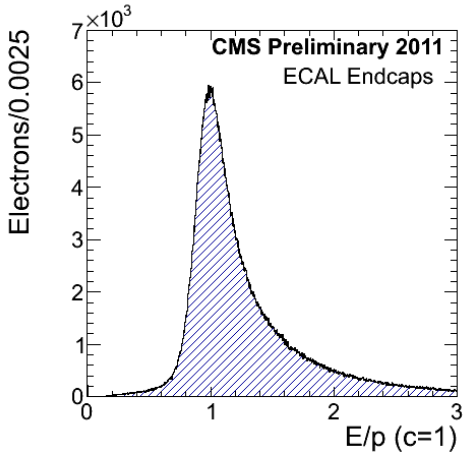


**Figure 3.** Template used in 2012 for the distribution of the fraction $E/p$ for the endcaps.

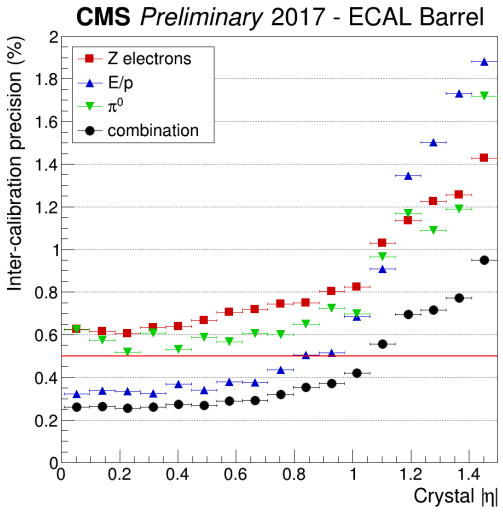


**Figure 4.** Final individual and combined inter-calibration precision for 2017.

The CMS tracker provides an independent measurement of the momentum of a charged particle by reconstructing its track and obtaining its curvature in the magnetic field. Specifically, the ratio $E/p$, where $E$ = ECAL supercluster energy (which depends on the inter-calibration factors) and $p$ = tracker momentum, should remain stable over time.

We first obtain the $E/p$ templates from a high purity sample of high energy electrons from $W/Z$ decay. These templates vary with $\eta$; one example template, used in 2012 for all endcap electrons, is shown in Fig. 3. Next, the inter-calibration coefficients are derived using an iterative approach which ensures that the observed $E/p$ distribution matches these templates:

$$C_i^{\text{N}} = C_i^{\text{N}-1} \times \frac{\sum_{\text{good electrons}} F_i \times P\left(E_{\text{SC}}^{\text{N}-1} | p_{\text{trk}}\right) \times \frac{p_{\text{trk}}}{E_{\text{SC}}^{\text{N}-1}}}{\sum_{\text{good electrons}} F_i \times P\left(E_{\text{SC}}^{\text{N}-1} | p_{\text{trk}}\right)} \quad (4)$$

where $N$ is the iteration index, $F_i$ is the fraction of the supercluster energy in crystal $i$, and $P\left(E_{\text{SC}} | p_{\text{trk}}\right)$ is the probability, found from the template, of depositing $E_{\text{SC}}$ in ECAL given that the tracker reconstructs momentum $p_{\text{trk}}$.

*3.3. Inter-calibration using $Z \to ee$*

In this technique, the inter-calibration constants are chosen such that the overall Z-peak, obtained from data in all crystals, yields the correct mass and lifetime.

We perform a maximum likelihood fit of the data to a Voigtian, a convolution of the natural $Z-$shape (which depends on $Z-$mass and lifetime), and a Gaussian spread due to resolution effects:

$$\mathcal{L} = \prod_{Z \to ee \text{ events}} \text{Voigt}\left(m_{ee}, \sigma_{ee}, M_Z, \Gamma_Z\right) \tag{5}$$

where

$$\begin{aligned} m_{e_1e_2} &= \sqrt{2 \times E_{\text{corrected}}\left(e_1\right) \times E_{\text{corrected}}\left(e_2\right) \times \left(1 - \cos\theta_{12}\right)} \\ \sigma_{e_1e_2} &= \frac{1}{2} \times M_Z \times \left(\frac{\sigma_E}{E}\left(e_1\right) \oplus \frac{\sigma_E}{E}\left(e_2\right)\right) \\ E_{\text{corrected}} &= \frac{E_{ECAL}}{r\left(\eta\right)} + E_{\text{preshower}} \end{aligned}$$

Here, $r\left(\eta\right)$ is an $\eta$-dependent correction which is equivalent to normalizing correctly between all bins in $\eta$.

The inter-calibration coefficients, which affect the reconstructed energy, are parameters of the fit; as a bonus, the energy resolution binned in $\eta$ is another parameter of the fit and can also be computed using this technique.

*3.4. Estimating inter-calibration uncertainty and combining measurements*

We have three independent measurements of the inter-calibration coefficients for each crystal. In order to combine the results, we first obtain estimates of the precision of each method. Assuming that the three measurements of the inter-calibrations are uncorrelated, we can relate the values to be determined – the uncertainty in each method individually – to the known spread in the distribution of the differences in the coefficients obtained with different methods:

$$\begin{aligned} \sigma_1^2 + \sigma_2^2 &= \sigma_{1-2}^2 \\ \sigma_1^2 + \sigma_3^2 &= \sigma_{1-3}^2 \\ \sigma_2^2 + \sigma_3^2 &= \sigma_{2-3}^2 \end{aligned} \quad \Longrightarrow \quad \begin{aligned} \sigma_1^2 &= \frac{1}{2}\left(\sigma_{1-2}^2 + \sigma_{1-3}^2 - \sigma_{2-3}^2\right) \\ \sigma_2^2 &= \frac{1}{2}\left(\sigma_{2-3}^2 + \sigma_{1-2}^2 - \sigma_{1-3}^2\right) \\ \sigma_3^2 &= \frac{1}{2}\left(\sigma_{1-3}^2 + \sigma_{2-3}^2 - \sigma_{1-2}^2\right) \end{aligned} \tag{6}$$

This provides estimates of the uncertainty due to each method individually. Note that both the statistical and systematic uncertainties are accounted for in this estimate of the factors $\sigma_i$.

The combined inter-calibration coefficient for each crystal is then obtained as the mean of the coefficients obtained by each individual method weighted by $1/\sigma_i^2$. The residual uncertainty in the inter-calibration coefficients is shown in Fig. 4. The precision from $Z \to ee$ and $\pi^0 \to \gamma\gamma$ decays is at the level of the systematic error, while the statistical errors are still dominant for the $E/p$ precision at $|\eta| > 1$. The black points represent the combined weighted precision. Note that for the endcaps in 2017, we only use the $Z \to ee$ method because it is much more precise than the other methods; therefore, we do not have numerical estimates of the precision in the endcaps. As shown, with the increased statistics available in 2017, the precision of the inter-calibration is now at the sub-percent level throughout the barrel.

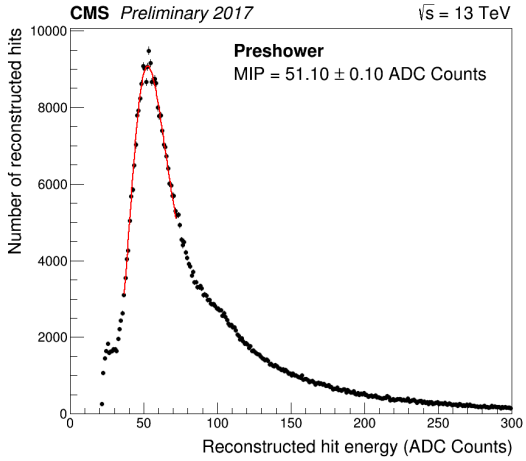


**Figure 5.** Example fit of the MIP peak in an ECAL preshower sensor.

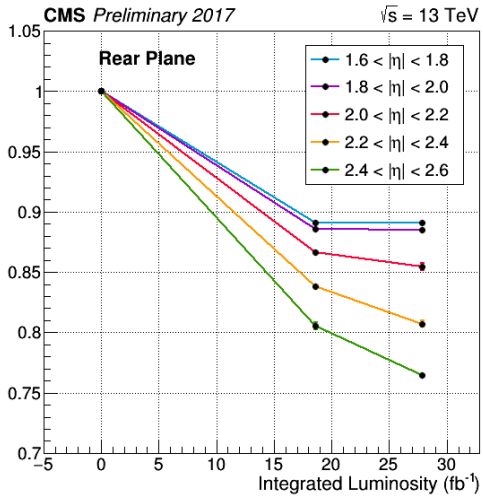


**Figure 6.** Degradation of the ECAL preshower MIP response during 2017 in the rear plane.

## 4. ECAL Preshower Energy Scale

In order to calibrate ECAL preshower, we take special runs once every few months with the preshower operated in high gain mode. This provides a measurement of the MIP peak for each ECAL preshower sensor; the distribution for each individual sensor is fitted to a Landau convoluted with a Gaussian. Since the readout from the sensors is in ADC counts, this gives the ADC-to-MIP conversion factor. The MIP peak for one example sensor is shown in Fig. 5. Next, using the fact that the MIP-to-GeV conversion factor is a material property which depends only on the thickness of the Si (1 MIP = 80.4 keV [7]), the ADC-to-GeV conversion factor is obtained and kept up-to-date with radiation damage. The evolution of the MIP response with respect to the beginning of 2017 is shown in Fig. 6. Note that the preshower only accounts for about 5% of the energy deposited by a particle in the endcaps, so this degradation does not significantly affect the energy resolution in the endcaps.

## 5. Monitoring and Validation

In the physics data reconstructed with up-to-date transparency corrections from the laser monitoring and with fresh calibrations, we monitor several well-understood physics quantities and ensure that these quantities are stable throughout the data-taking period. To monitor the energy scale, we use the $\pi^0$ resonance and $Z \to ee$ events; to monitor shower shapes, we use $Z \to ee$ events.

### *5.1. Monitoring energy scale using $\pi^0$ resonance*

The invariant mass distribution of $\pi^0$ decays is monitored continuously and is observed to be stable throughout the 2017 data-taking period, as shown in Fig. 7. The gaps in these plots are periods in which LHC was not running – note the recovery in the crystal transparency over those gaps. This figure also illustrates the necessity of continuous laser monitoring and transparency corrections, without which the energy scale would fluctuate by several percent over the course of the data-taking.

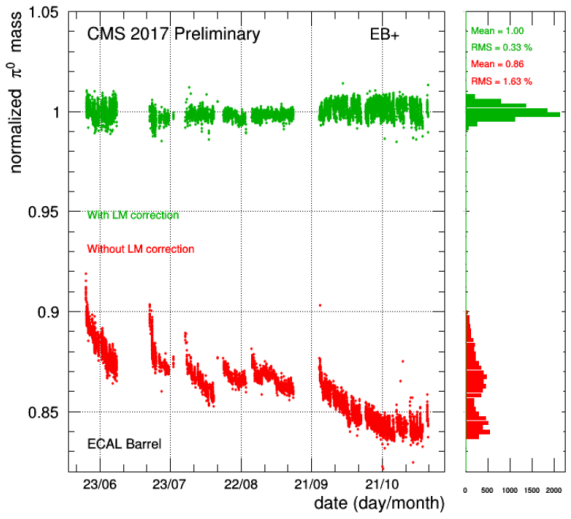


**Figure 7.** Relative energy scale measured from the invariant mass distribution of $\pi^0 \to \gamma\gamma$ decays, shown with and without laser monitoring (LM) correction.

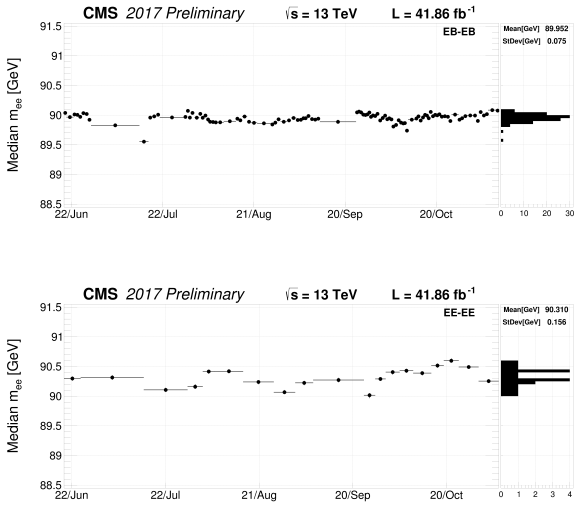


**Figure 8.** Reconstructed mass of the $Z \to ee$ peak during the 2017 data-taking period.

*5.2. Monitoring energy scale using $Z \to ee$ events*

The reconstructed mass of the $Z$-boson is monitored continuously and is also observed to be stable throughout 2017, as shown in Fig. 8, for events with both electrons in the barrel (top plot) and for events with both electrons in the endcaps (bottom plot).

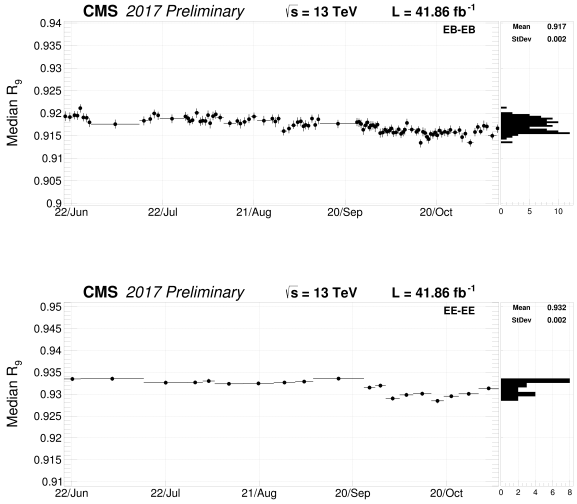


**Figure 9.** Reconstructed $R_9$ of electrons from $Z$-decays during the 2017 data-taking period.

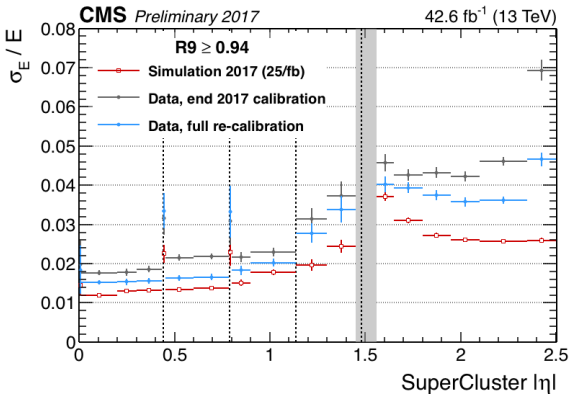


**Figure 10.** Improvement in energy resolution of ECAL with the latest intercalibrations (blue) versus with an older version (grey).

*5.3. Monitoring shower shape using $Z \to ee$ events*

The variable $R_9$ is often used in CMS physics analyses. It is defined as:

$$R_9 \equiv \frac{E_{3\times3}}{E_{SC}} \tag{7}$$

where $E_{3\times3}$ is the energy deposited in a ($3 \times 3$ crystal) region around the shower maximum, and $E_{SC}$ is the energy deposited in the full supercluster. Electromagnetic showers from electrons and photons are typically contained within a ($3 \times 3$ crystal) region, and $R_9$ is close to 1 for such showers. Scintillation deposits from hadronic showers, on the other hand, are generally spread out over many more crystals; for such showers $R_9$ is typically much lower. $R_9$ can therefore be used to discriminate between ECAL deposits originating from hadronic and electromagnetic showers.

The reconstructed $R_9$ of individual electron deposits from $Z \to ee$ events over the 2017 data-taking period is shown in Fig. 9, for events with both electrons in the barrel (top plot) and for events with both electrons in the endcaps (bottom plot), and is observed to be stable throughout the year.

## 6. Performance of the 2017 calibration

The $\eta-$binned energy resolution can be obtained using the same technique used to derive inter-calibration coefficients using $Z \to ee$ events, as discussed in section 3.3. During regular data-taking, the laser transparency corrections, pedestals, timing, and other low-level parameters of the reconstruction are generally set to their latest values, but the inter-calibrations are only typically updated once every few months. All data is generally reconstructed using the latest inter-calibrations a few months after the end of a data-taking period. Fig. 10 shows a significant improvement in energy resolution after applying the latest inter-calibration factors – the resolution remains better than 3.5% for barrel electrons.

## 7. Conclusions

The LHC physics program has been highly successful, with CMS playing a key role in the Higgs discovery and continuing to impose ever-tighter constraints on new physics. The CMS electromagnetic calorimeter plays a crucial role in these analyses and continues to operate extremely well despite the challenging conditions. The high statistics made available in Run II provides precise measurements of the inter-calibration coefficients in the energy reconstruction of ECAL, maintaining its excellent energy resolution. The monitoring and validation program continues to ensure that all measurements from ECAL are precise, dependable, and stable.

## References

[1] [CMS Collaboration] 2008 The CMS experiment at the CERN LHC *JINST* **3** S08004
[2] [Khachatryan, Vardan et al.] 2015 Performance of Electron Reconstruction and Selection with the CMS Detector in Proton-Proton Collisions at $\sqrt{s} = 8$ TeV *JINST* **10** P06005
[3] [Adzic, P. et al.] 2006 Reconstruction of the signal amplitude of the CMS electromagnetic calorimeter *Eur. Phys. J. C* **46 S1** 23-35
[4] [M. Anfreville et al.] 2008 Laser monitoring system for the CMS lead tungstate crystal calorimeter *Nuclear Instruments and Methods in Physics Research, A* **594** 2:292-320
[5] [CMS Collaboration] 2013 Energy calibration and resolution of the CMS electromagnetic calorimeter in pp collisions at $\sqrt{s} = 7$ TeV *JINST* **09** P09009
[6] [Meridiani, Paolo and Paramatti, Riccardo] 2006 Use of $Z \to e^+e^-$ events for ECAL calibration *CMS-NOTE-2006-039*
[7] [Particle Data Group] 2016 Review of Particle Physics, 2016-2017 *Chin. Phys. C* **10** 40:100001